

Reconfigurable locally resonant surface acoustic demultiplexing behavior in ZnO-based phononic crystal

Cite as: J. Appl. Phys. **129**, 024901 (2021); <https://doi.org/10.1063/5.0024485>

Submitted: 08 August 2020 . Accepted: 17 December 2020 . Published Online: 08 January 2021

F. Taleb,  S. Darbari, and  A. Khelif



View Online



Export Citation



CrossMark

ARTICLES YOU MAY BE INTERESTED IN

[Subwavelength confinement of propagating surface acoustic waves](#)

Applied Physics Letters **118**, 013502 (2021); <https://doi.org/10.1063/5.0038381>

[Three-dimensional phononic crystal with ultra-wide bandgap at megahertz frequencies](#)

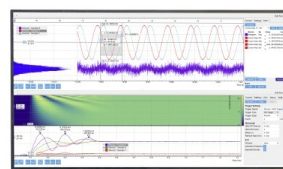
Applied Physics Letters **118**, 063507 (2021); <https://doi.org/10.1063/5.0033615>

[An elastic higher-order topological insulator based on kagome phononic crystals](#)

Journal of Applied Physics **129**, 035102 (2021); <https://doi.org/10.1063/5.0031377>

Challenge us.

What are your needs for
periodic signal detection?



Zurich
Instruments




Reconfigurable locally resonant surface acoustic demultiplexing behavior in ZnO-based phononic crystal

Cite as: J. Appl. Phys. **129**, 024901 (2021); doi: [10.1063/5.0024485](https://doi.org/10.1063/5.0024485)

Submitted: 8 August 2020 · Accepted: 17 December 2020 ·

Published Online: 8 January 2021



F. Taleb,¹ S. Darbari,^{1,a)}  and A. Khelif² 

AFFILIATIONS

¹Nano Sensors and Detectors Lab. and Nano Plasmophotonic Research Group, Faculty of Electrical and Computer Engineering, Tarbiat Modares University, Tehran 1411713116, Iran

²FEMTO-ST Institute, UBFC, CNRS, ENSMM, UTBM, 15B Avenue des Montboucons, 25030 Besançon, France

^{a)}Author to whom correspondence should be addressed: s.darbari@modares.ac.ir

ABSTRACT

We present the design and numerical investigation of a reconfigurable and miniature locally resonant surface acoustic wave demultiplexer based on a ZnO pillar phononic crystal, for the first time. Hollow cylinder line defects are used as waveguides, due to their good structural controllability over the local resonant waveguiding frequency and bandwidth. Two local resonant surface acoustic waveguides are designed and simulated as the output channels of the demultiplexer, and the shear-horizontal wave transmission spectra are calculated for each channel individually. The designed radio frequency demultiplexing output channels support frequencies of 4.14 GHz and 4.28 GHz, with respective bandwidths of 40 MHz and 60 MHz, while their spatial separation is just about 800 nm. In order to achieve a reconfigurable output characteristic, the effect of acoustoelectric interaction in piezoelectric semiconductors is numerically simulated in this study. The acoustoelectric interaction causes an additional stiffness in ZnO that can be released by adding extra charge carriers, i.e., increasing conductivity, thus changing the effective elasticity of the ZnO structures and the guiding frequencies of the output channels. Two output frequencies show red shifts of about 100 MHz and 150 MHz by extremely increasing the conductivity of ZnO structures from 0.01 S/m to 100 S/m.

Published under license by AIP Publishing. <https://doi.org/10.1063/5.0024485>

I. INTRODUCTION

Reflection and isolation of elastic/acoustic waves in phononic crystals (PNCs), which consist of a periodic array of scatterers, have led to many applications for PNCs in waveguides, resonators, energy harvesters, telecommunication filters, couplers, demultiplexers, and also sensors.^{1–12} On the other hand, surface acoustic wave (SAW) devices have shown promising applications, ranging from various sensing fields to the signal processing and wireless telecommunication fields, such as RF filters and duplexers.^{13–18} PNCs, in certain conditions, can create bandgaps for SAWs as well.^{19–22} Bragg bandgap, as a result of Bragg scattering from PNCs, occurs at a frequency that is dependent on the lattice constant of PNCs. However, local resonance bandgaps, first introduced in 2000 by Liu *et al.*,²³ are a type of bandgap opening at lower frequency ranges than the Bragg bandgap frequency range, without the need for an

increased lattice constant. In fact, in a periodic array of locally resonant scatterers (such as pillars), a new set of low-frequency elastic modes, named as surface coupled modes, are created, due to which, in their absence, the local resonance bandgaps open. Recent reports have shown the emergence of local resonance bandgaps for PNCs, made of various resonators, both numerically and experimentally.^{24–26} Introducing defects inside such PNCs can be utilized to localize SAWs to defect structures. The introduced defects can be designed so that guiding modes are created inside the local resonance bandgap, which can be used as SAW waveguides.^{27–29}

Acoustoelectric interaction, which was introduced in 1953,³⁰ occurs during the propagation of elastic waves in piezoelectric semiconductor materials. This phenomenon modifies the velocity, amplitude, and phase of the elastic wave, since the reverse piezoelectric effect creates an additional stiffness in the medium as a result of bounded charges induced by the propagating elastic wave.

In other words, the elasticity of the piezoelectric medium increases effectively as a result of elastic wave propagation.³¹ This extra stiffness can be partially released by inducing excess charge carriers into the material (by UV illumination, etc.), which can screen the bounded charge's field, and modulating the elastic wave's velocity, amplitude, and phase. This interaction has found various applications in SAW-based sensors, such as UV detectors.^{32–34} Consequently, the acoustoelectric effect can be utilized to induce effective changes in the elasticity of piezoelectric semiconductor materials. Thus, we benefit from the acoustoelectric interaction to introduce tunability to the behavior of SAW-based devices constructed from piezoelectric materials. Regarding this, we have recently reported a tunable locally resonant SAW filter, consisting of a ZnO-based PNC.³⁵ In this line of research, here we present, for the first time, the design and numerical investigation of a miniature SAW demultiplexer device based on local resonance bandgaps in a PNC of ZnO resonators. Moreover, the proposed device is designed in such a way that it shows switchable output frequencies in response to the conductivity modulation of ZnO resonators. The use of hollow cylinder line defects to achieve waveguides with controllable bandwidth and frequency also adds to the prominence in this work. The PNC in this device is assumed to be made of ZnO resonators, which is a piezoelectric semiconductor with strong acoustoelectric interaction, and benefits from a simple, low cost, and CMOS compatible fabrication process. The output transmission peak frequencies of the demultiplexer device are demonstrated to have an effective red shift in response to the increased conductivity of the ZnO structures. Realization of the presented reconfigurable frequency behavior is proposed to be achieved by UV illumination after the fabrication process, which is a contactless and simple approach. The proposed reconfigurable demultiplexer device works in the GHz frequency domain and, thus, can be considered a promising platform for analog signal processing in wireless communication systems.

II. PHYSICAL PRINCIPLES AND STRUCTURE

Line defects in the proposed PNC can create guiding modes inside the local resonance bandgaps, allowing the transmission of certain frequencies. The value and number of the defect guiding frequencies depend on the elastic and structural parameters of the defect resonators. A schematic of the proposed demultiplexer as well as its top view are shown in Fig. 1, wherein the input and two output ports are highlighted. Here, we propose a PNC-based demultiplexer device on Si consisting of ZnO resonators, and their elastic parameters can be controlled through the acoustoelectric effect, which will result in a switchable output frequency behavior. The acoustoelectric-induced tunability is proposed to be achieved through contactless UV illumination (as shown in Fig. 1) in practice. Hollow cylinder defects are used as waveguiding resonators, since we have shown that they provide an acceptable designing degree of freedom in their structural parameters to control the corresponding transmission width and frequencies.³⁵ A defect with a hollow cylinder of high outer radius can have a wide transmission, and by changing the inner to outer radii ratio, one can modify the frequency behavior. On the other hand, line defects with hollow cylinders of smaller outer radius and high inner to outer radii ratio

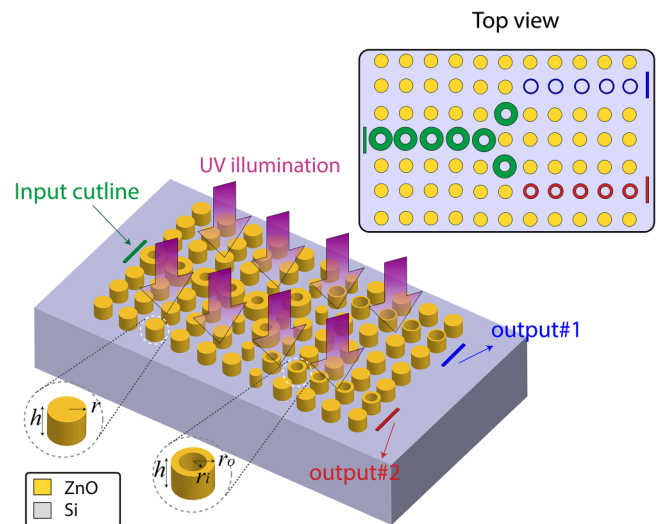


FIG. 1. The schematic of the proposed SAW demultiplexer device and the top view, with one input (green channel) and two output channels (red and blue channels), made of hollow cylinder line defects in a ZnO-based pillar PNC. UV illumination is proposed to create the reconfigurable demultiplexing behavior.

create narrow-band transmission spectra, making them suitable choices for output waveguides of the demultiplexer device. The elastic wave equations have been solved through the finite element method (FEM) to extract the band structures and transmission spectra of the designed device. More details on the elastic wave propagation equations, coupled with acoustoelectric interaction, are given elsewhere.³⁵

III. RESULTS AND DISCUSSION

The proposed demultiplexer device consists of a PNC made from ZnO pillars in a square lattice with radius (r), height (h), and lattice constant (a) of 65 nm, 100 nm, and 200 nm, respectively, over a Si substrate. In order to design the demultiplexer waveguides, first we have investigated the transmission spectra of the hollow cylinder waveguides with r_o values of 95 nm and 65 nm and different r_i/r_o ratios. We have extracted the guiding central frequency (f_d) and the relating full width at half maximum (FWHM) (illustrated by error bars), as depicted in Fig. 2. The blue dotted level represents the midgap level, and the gray bottom and top regions display the transmission zones where the bandgap lies between them. Our goal is to choose two narrow-band waveguides as the output channels, with minimum possible frequency overlapping spectra, occurring in the input waveguide GHz frequency range. We have numerically investigated different demultiplexer designs based on the different waveguides (Fig. 2); however, the results show that mostly the elastic impedance mismatch between the input and output waveguides leads to destructive reflections at the junction of the demultiplexer, preventing efficient wave coupling from the input channel to the outputs. Our results indicate that an input waveguide consisting of hollow cylinders with

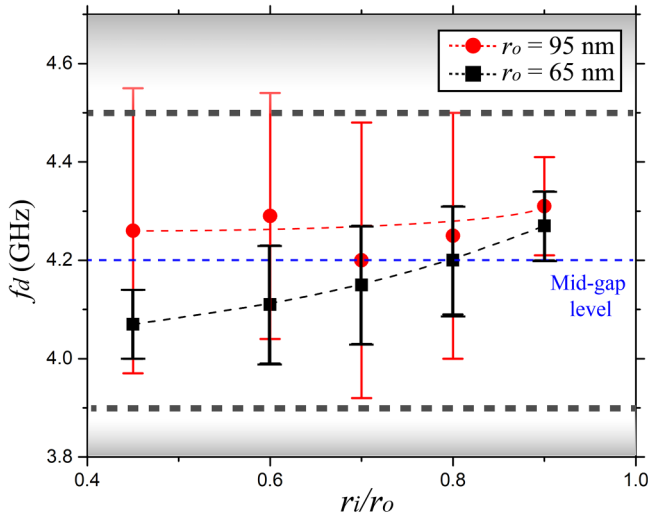


FIG. 2. f_d and FWHM values (shown by error bars) of transmission spectra for local resonant guiding modes with $r_o = 95$ nm (red) and $r_o = 65$ nm (black) vs different r_i/r_o values.

$r_o = 95$ nm and $r_i/r_o = 0.45$, and output waveguides with $r_o = 65$ nm and different r_i/r_o ratios of 0.7 and 0.9, show an acceptable demultiplexing behavior that is in agreement with the observed frequency behaviors in Fig. 2.

Figures 3(a)–3(d) show the geometries of the unit cell and supercells used to calculate the band structures of the perfect PNC [the first Brillouin zone (BZ) is shown as the inset] and line defect waveguides, while the periodic boundary condition (PBC) is applied on the sidewalls of the substrate. Corresponding to the perfect PNC band structure, to calculate the band structure for the super cells relating to the line defected PNCs [Figs. 3(b)–3(d)], we run an eigenfrequency study with Bloch PBC applied on the sidewalls of the supercells and sweep the wave vector (k) between zero and π/a (“ a ” is the lattice constant of PNC) for the ΓX direction. The calculated band structures of the perfect PNC and the designed input and two output waveguides are depicted in Figs. 3(e)–3(h). The perfect PNC band structure [Fig. 3(e)] shows a Bragg bandgap around 12 GHz (green ribbon) and two low-frequency local resonance bandgaps (blue ribbons) occurring between a range of 8–9 GHz and 3.98–4.5 GHz. Figures 3(f)–3(h) depict the magnified band structures of input and two output waveguides around the first low-frequency local resonance bandgap (3–6 GHz) in the Γ -X direction of the first Brillouin zone in order to observe all possible created guiding modes. The defect-induced guiding modes are shown by red bands, some of which locate inside the bandgap.

In the next step, the transmission spectra of the designed three waveguides are calculated using a 11×11 PNC, as shown in Fig. 4(a). The calculation is done by dividing the average absolute displacement components in x , y , and z directions over the output cutline by similar values over the input cutline, as shown by the red lines in Fig. 4(a). It is notable that we focus on the transmission of the shear-horizontal wave, due to its high velocity, high effective

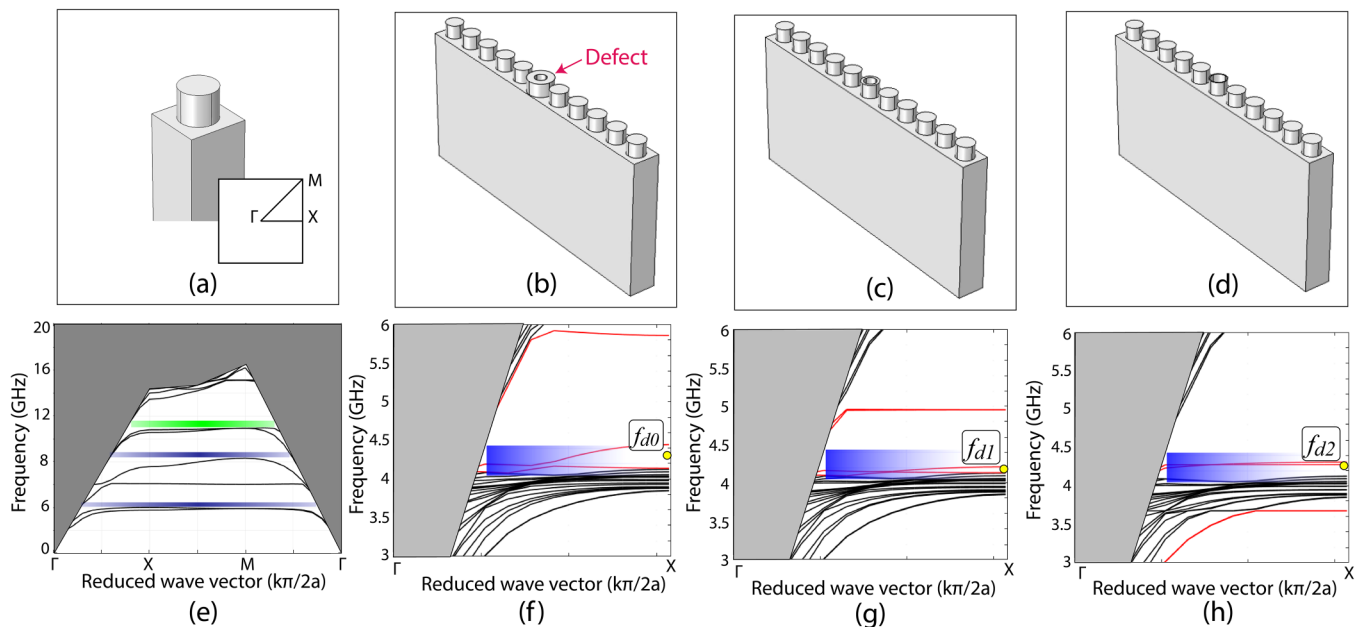


FIG. 3. The geometry of the PNC’s unit cell and the first BZ are shown in part (a). The supercells for the designed (b) input and (c)–(d) output waveguides used for band structure calculations are depicted. Band structures of (e) the perfect pillar-based PNC and the supercells of hollow cylinder line defects in Γ -X direction with (f) $r_o = 95$ nm and $r_i/r_o = 0.45$, (g) $r_o = 65$ nm and $r_i/r_o = 0.7$, and (h) $r_o = 65$ nm and $r_i/r_o = 0.9$.

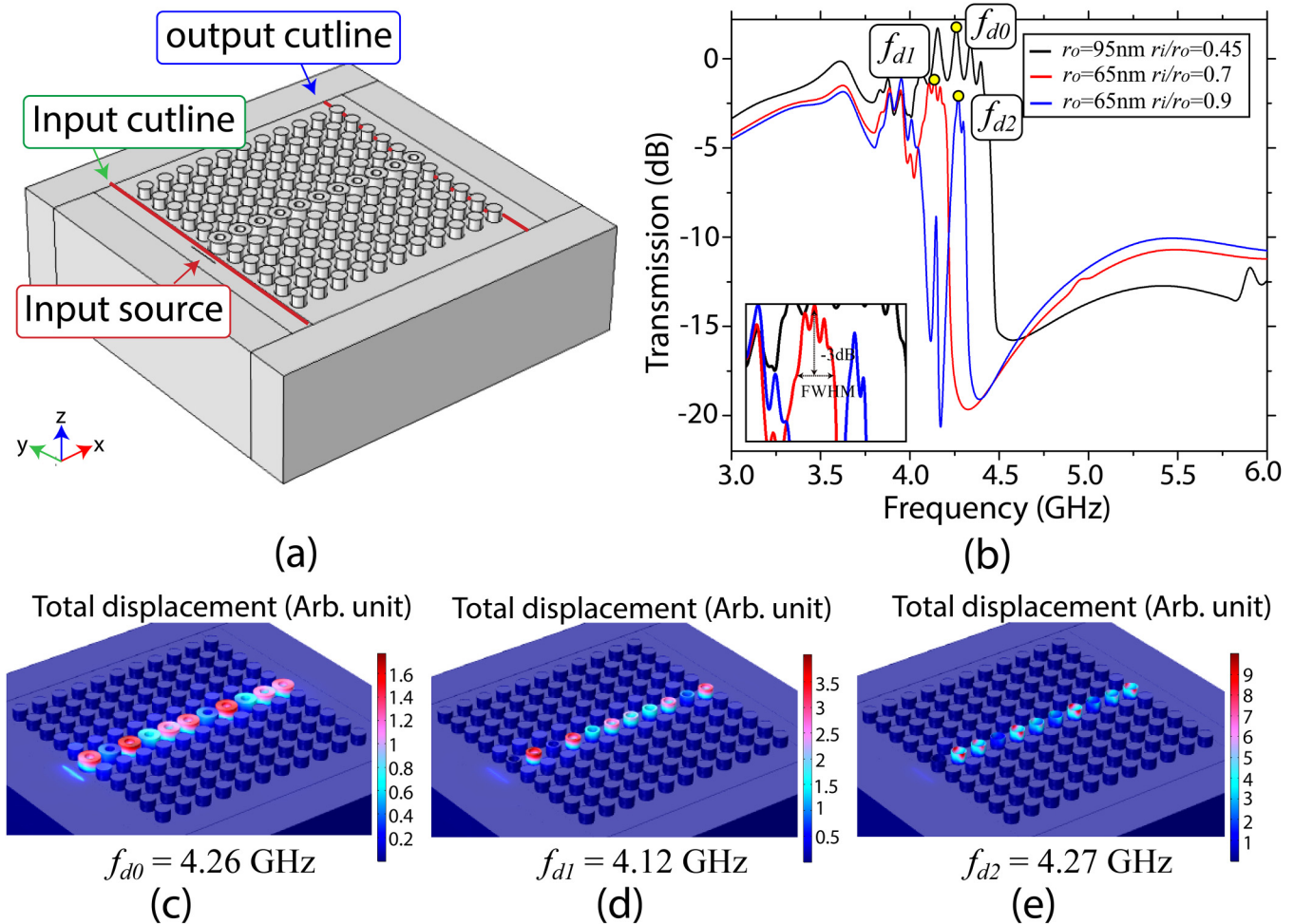


FIG. 4. (a) An 11×11 PNC with a linear hollow cylinder defect for calculation of the waveguiding transmission spectra. (b) Shear-horizontal transmission spectra for waveguides with $r_o = 95$ nm and $r_i/r_o = 0.45$ (black), $r_o = 65$ nm and $r_i/r_o = 0.7$ (red), and $r_o = 65$ nm and $r_i/r_o = 0.9$ (blue). Total displacement in the designed waveguides at central guiding frequencies, corresponding to part (c) $f_{d0} = 4.26$ GHz, (d) $f_{d1} = 4.12$ GHz, and (e) $f_{d2} = 4.27$ GHz.

electromechanical coupling factor, and high energy concentration near the surface. Three transmission spectra for the discussed hollow cylinder waveguides in Figs. 3(f)–3(h) are superimposed in Fig. 4(b). The inset of Fig. 4(b) demonstrates how FWHM is calculated for a magnified transmission peak, in which the difference of two -3 dB frequencies from both sides of the central frequency is defined as FWHM. As can be seen in the figure, the input waveguide transmission spectrum successfully supports two individual output frequency spectra or covers both the output waveguide bandwidths ($\text{FWHM}_{\text{in}} > \text{FWHM}_{\text{out1}} + \text{FWHM}_{\text{out2}}$). Also, the output waveguides are designed to support narrow bandwidths, and distinguishable transmission spectra with minimal overlapping ($f_{d1} - f_{d2} > \text{FWHM}_{\text{out1}} + \text{FWHM}_{\text{out2}}$), which is required to suppress the crosstalk between the output channels of the proposed demultiplexer.

The observed slight gain in the black transmission curve in part (b) can be attributed to the negative slope of the relating guiding

bands, as shown in Fig. 3(f), which can result in wave phenomena such as negative refraction or superlens effect in phononic metamaterials.^{36,37} These phenomena can create transmission gain in certain frequencies. However, elaborating these issues is beyond the scope of this article. Figures 4(c)–4(e) demonstrate the total displacement for the central guiding frequencies of $f_{d0} = 4.26$ GHz, $f_{d1} = 4.12$ GHz, and $f_{d2} = 4.27$ GHz, corresponding to Figs. 3(f)–3(h) and 4(b). It can be observed that the total displacement in part (e) shows a whispering gallery mode inside the local resonance gap, since hollow cylinders with high r_i/r_o values allow the creation of these modes with nearly flatband guiding modes and narrow-band transmission spectra.

Finally, the designed waveguides are assembled together to achieve a locally resonant demultiplexer, wherein the ZnO structures are considered to be intrinsic. The designed demultiplexer geometry and its top view are presented in Figs. 5(a) and 5(b), respectively,

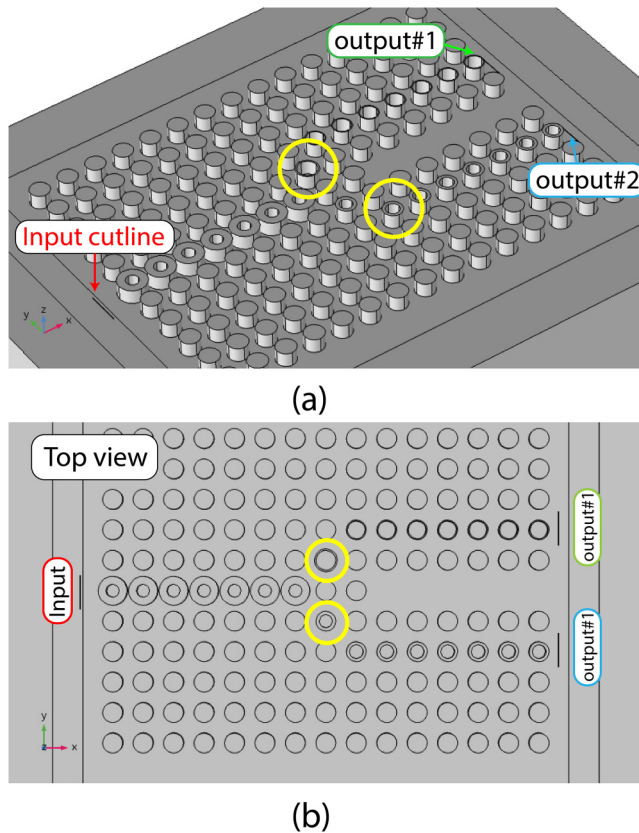


FIG. 5. (a) The geometry of the 11×15 demultiplexer with an input and two output waveguides, consisting of hollow cylinders, with a Y-junction between them (marked by yellow circles). The input and output cutlines are shown in the picture. (b) Top view of the same device.

wherein the input and two output cutlines are highlighted. In order to enhance the wave coupling between the input and output waveguides, we have optimized the inner and outer radii of Y-junction hollow cylinders (shown by the yellow circle). Thus, we have chosen r_o values of upper and bottom Y-junction hollow cylinder to be equal to 75 nm and 65 nm with r_i/r_o of 0.85 and 0.65, respectively. Moreover, in order to reduce the crosstalk between the output waveguides, with a spacing of about 800 nm, we have removed the intermediate row of pillars, as shown in Fig. 5. To calculate the shear-horizontal transmission of each output port, the averaged absolute displacement components over each output cutline are divided by the similar values over the input cutline. In order to prove the reconfigurable behavior of the designed demultiplexer, we have considered two cases, in which the conductivity (σ) of ZnO is changed from an intrinsic value of 0.01 S/m to 100 S/m. It should be noted that ZnO is a wide bandgap semiconductor with extensively low carrier concentration and conductivity in its intrinsic form. However, UV illumination, and the consequent photogenerated carriers, can increase the conductivity intensively. On the other hand, oxygen molecules naturally tend to be adsorbed on a ZnO

surface and lead to the formation of an electron-depleted surface region, which allows intensive photoconductive response to UV illumination in ZnO structures.^{38–40}

Moreover, considering that the UV penetration depth in ZnO is about 180 nm, we have considered a uniform impact of UV on all of the ZnO structures and have ignored the acoustoelectric effect in Si because of its centrosymmetric nature. Details of acoustoelectric formalism for modulation in the elastic parameters of ZnO upon conductivity modulation can be found in our previous work,³⁵ wherein the relating loss is accounted by the complex effective stiffness and wave number, leading to a decaying propagating wave.⁴¹ It is worth mentioning that the propagation loss is maximized at the conductivity of about $\sigma \sim 7$ S/m for ZnO, where the propagation velocity equals the average velocity of the open and short-circuit cases.⁴² Hence, the acoustoelectric loss is not significant in our proposed switching conductivities. Figures 6(a) and 6(b) demonstrate the transmission spectra of the two output ports, for $\sigma = 0.01$ S/m and $\sigma = 100$ S/m, respectively. For the intrinsic ZnO, two output transmissions are observed at $f_{d1} = 4.14$ GHz (red) and $f_{d2} = 4.28$ GHz (black) with respective peak intensities of -11.03 and -11.15 dB, and a crosstalk of about -9 dB, as shown in part (a). By increasing the conductivity value of ZnO, the guiding frequencies show a red shift to $f_{d1} = 4.05$ GHz and $f_{d2} = 4.13$ GHz with the respective peak intensities of -10.16 dB and -9.11 dB, and a crosstalk of about -10.6 dB [shown in part (b)].

The observed red shift is attributed to the release of acoustoelectric-induced extra piezoelectric stiffness in ZnO structures, due to screening of the excess carrier field. The maximum achieved red shifts upon increasing σ from 0.01 S/m to 100 S/m are $\Delta f_{d1} \approx 100$ MHz and $\Delta f_{d2} \approx 150$ MHz. Figures 6(c) and 6(d) demonstrate the total displacement in the corresponding output channels for f_{d1} and f_{d2} ($\sigma = 0.01$ S/m), respectively. It is observed that the elastic wave is frequency-selectively localized in the output waveguides successfully. The inevitable reflections from the boundaries can be responsible for the observed non-uniform total displacement distribution at a number of hollow cylinders. We should mention that most of the displacement is localized to the waveguide's hollow cylinders at their resonance frequencies, being maximum at the upper edge and minimum near the substrate surface. Moreover, it should be noted that the leaked displacement into the substrate surface is not comparable to the hollow cylinder's displacement.

Since it is well established that output frequency characteristics, such as bandwidth and resonance frequency, are highly dependent on the structural parameters of the resonators in local resonance waveguides, we investigate the dependence of the reported demultiplexing behavior on the possible tolerances of the structural parameters during the fabrication process. In this regard, first we have investigated the case with random radius tolerances in output and input waveguides. Our results show that a maximum dimension tolerance of 5 nm in the outer radius of a maximum number of three hollow cylinders in output and input waveguides is acceptable. However, there are some critical structural aspects in the designed structure, such as the sidewall slopes of the hollow cylinders, wherein such fabrication tolerances degrade the output significantly. Thus, vertical etching of the nanoscale hollow cylinders should be performed with special care

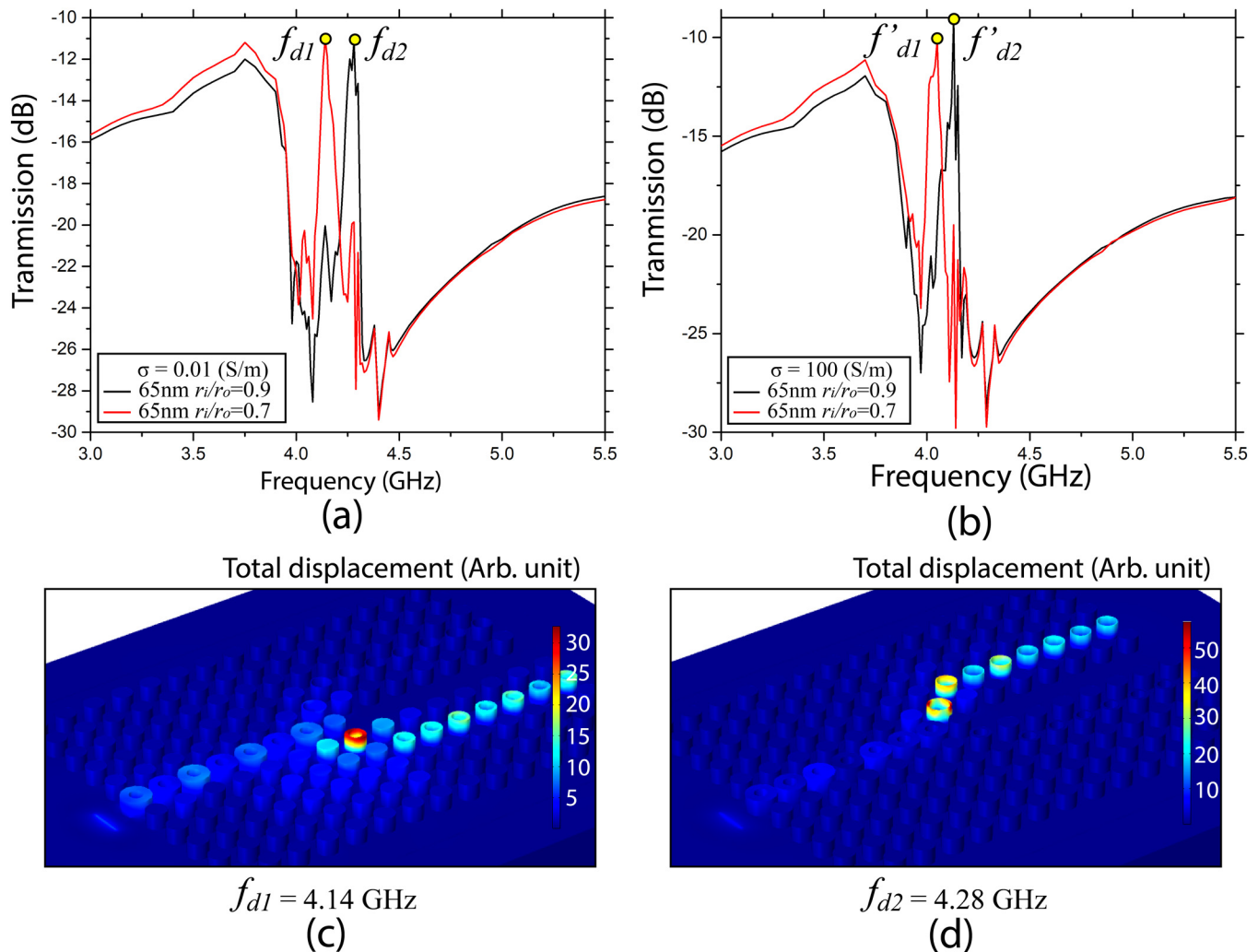


FIG. 6. Shear-horizontal transmission spectra for two outputs at (a) $\sigma = 0.01$ S/m and (b) $\sigma = 100$ S/m. The magnified transmission peaks are shown in the figure insets. The total displacement in the demultiplexer device for $\sigma = 0.01$ S/m at central guiding frequencies of (c) $f_{d1} = 4.14$ GHz and (d) $f_{d2} = 4.28$ GHz.

and by high precision procedures.^{43,44} Moreover, studying the systematic variations in the critical dimensions, we have scaled up/down the in-plane dimensions of the design for $\pm 5\%$ and show that the central peak frequencies change inversely by the scaling factor and the peak intensities show an overall drop between 1 and 3 dB, which is acceptable.

IV. CONCLUSION

We present the design and numerical investigation of a miniature and reconfigurable SAW local resonant demultiplexer working in a GHz frequency domain, benefiting from acoustoelectric interaction. The presented device is based on a PNC made of ZnO pillars, while ZnO hollow cylinder line defects serve as the input and two output waveguides as the demultiplexer channels. For a

successful design, we have benefited from the allowed degree of freedom in designing the structural parameters of the hollow cylinders over their waveguiding characteristics. In our design, output central frequencies are 4.14 GHz and 4.28 GHz, with FWHM values of 40 MHz and 60 MHz, respectively. The proposed miniature PNC-based SAW demultiplexer allows a crosstalk of about 10 dB between the output channels, while the output interspacing is just about 800 nm. Benefiting from acoustoelectric interaction, by increasing the conductivity of ZnO structures from an intrinsic value of 0.01 S/m to 100 S/m, red shifts of 100 MHz and 150 MHz are achieved for the designed guiding frequencies. Thus, the designed local resonant SAW demultiplexer is proved to have a switchable frequency behavior. The proposed device is promising for SAW-based wireless communication applications such as reconfigurable RF duplexers.

ACKNOWLEDGMENTS

The authors acknowledge the partial financial support from the Iran National Science Foundation (Grant No. 97010601) and the financial support from the Tarbiat Modares University through Grant No. 39703.

DATA AVAILABILITY

The data that support the findings of this study are available from the corresponding author upon reasonable request.

REFERENCES

- ¹R. H. Olsson, M. Ziaei-Moayyed, B. Kim, C. Reinke, M. F. Su, P. Hopkins, Y. M. Soliman, D. F. Goettler, Z. C. Leseman, and I. El-Kady, in *2011 IEEE International Ultrasonics Symposium* (IEEE, 2011), pp. 983–988.
- ²S. Mohammadi, A. Eftekhar, A. Khelif, W. Hunt, and A. Adibi, *Appl. Phys. Lett.* **92**, 221905 (2008).
- ³F. Shu, Y. Liu, J. Wu, and Y. Wu, *Ultrasonics* **71**, 172–176 (2016).
- ⁴M. Ghasemi Baboly, C. M. Reinke, B. A. Griffin, I. El-Kady, and Z. C. Leseman, *Appl. Phys. Lett.* **112**, 103504 (2018).
- ⁵M. Ghasemi Baboly, A. Raza, J. Brady, C. M. Reinke, Z. C. Leseman, and I. El-Kady, *Appl. Phys. Lett.* **109**, 183504 (2016).
- ⁶S. Mohammadi, A. Eftekhar, R. Pourabolghasem, and A. Adibi, *Sens. Actuators A Phys.* **167**, 524–530 (2011).
- ⁷A. Shakeri, S. Darbari, and M. K. Moravvej-Farshi, “Designing a tunable acoustic resonator based on defect modes stimulated by selectively biased PZT rods in a 2D phononic crystal,” *Ultrasonics* **92**, 8–12 (2019).
- ⁸M. Javadi, A. Heidari, and S. Darbari, *Curr. Appl. Phys.* **18**, 361–368 (2018).
- ⁹H. Shin, J. A. Cox, R. Jarecki, A. Starbuck, Z. Wang, and P. T. Rakich, *Nat. Commun.* **6**, 6427 (2015).
- ¹⁰Y. Pennec, B. Djafari-Rouhani, J. O. Vasseur, A. Khelif, and P. A. Deymier, *Phys. Rev. E* **69**, 046608 (2004).
- ¹¹B. Rostami-Dogolsara, M. Moravvej-Farshi, and F. Nazari, *IEEE Trans. Ultrason. Ferroelectr. Freq. Control* **63**, 1468–1473 (2016).
- ¹²A. Mehaney, *Ultrasonics* **93**, 37–42 (2019).
- ¹³M. Lewis, “SAW filter employing interdigitated interdigital transducers IIDT,” in *1982 Ultrasonics Symposium* (IEEE, 1982), pp. 12–17.
- ¹⁴J. Filipiak, A. Kawalec, and E. Danicki, *Ultrasonics* **28**, 355–357 (1990).
- ¹⁵J. Tsutsumi, S. Inoue, Y. Iwamoto, T. Matsuda, M. Miura, Y. Satoh, M. Ueda, and O. Ikata, in *Proceedings of the 2003 IEEE International Frequency Control Symposium and PDA Exhibition Jointly with the 17th European Frequency Control Time Forum* (IEEE, 2003), pp. 861–867.
- ¹⁶M. Kadota, T. Nakao, N. Taniguchi, E. Takata, M. Mimura, K. Nishiyama, T. Hada, and T. Komura, *Jpn. J. Appl. Phys.* **44**, 4527–4531 (2005).
- ¹⁷Y. Roh and S. Lee, *Ultrasonics* **42**, 413–416 (2004).
- ¹⁸H. Xu, S. Dong, W. Xuan, U. Farooq, S. Huang, M. Li, T. Wu, H. Jin, X. Wang, and J. Luo, *Appl. Phys. Lett.* **112**, 093502 (2018).
- ¹⁹X. Zhang, T. Jackson, E. Lafond, P. Deymier, and J. Vasseur, *Appl. Phys. Lett.* **88**, 041911 (2006).
- ²⁰Y. Tian, H. Li, Y. Ke, C. Yuan, and S. He, *IEEE Trans. Ultrason. Ferroelectr. Freq. Control* **63**, 757–763 (2016).
- ²¹K. Kokkonen, M. Kaivola, S. Benchabane, A. Khelif, and V. Laude, *Appl. Phys. Lett.* **91**, 083517 (2007).
- ²²D. M. Profunser, E. Muramoto, O. Matsuda, O. B. Wright, and U. Lang, *Phys. Rev. B* **80**, 014301 (2009).
- ²³Z. Liu, X. Zhang, Y. Mao, Y. Y. Zhu, Z. Yang, C. T. Chan, and P. Sheng, *Science* **289**, 1734–1736 (2000).
- ²⁴A. Khelif, Y. Achaoui, S. Benchabane, V. Laude, and B. Aoubiza, *Phys. Rev. B* **81**, 214303 (2010).
- ²⁵Y. Achaoui, A. Khelif, S. Benchabane, L. Robert, and V. Laude, *Phys. Rev. B* **83**, 104201 (2011).
- ²⁶B. Ash, S. Worsfold, P. Vukusic, and G. Nash, *Nat. Commun.* **8**, 174 (2017).
- ²⁷S. Benchabane, O. Gaiffe, R. Salut, G. Ulliac, V. Laude, and K. Kokkonen, *Appl. Phys. Lett.* **106**, 081903 (2015).
- ²⁸Y. Liu, A. Talbi, P. Pernod, and O. B. Matar, *J. Appl. Phys.* **124**, 145102 (2018).
- ²⁹Y. Guo, M. Schubert, and T. Dekorsy, *J. Appl. Phys.* **119**, 124302 (2016).
- ³⁰R. Parmenter, *Phys. Rev.* **89**, 990 (1953).
- ³¹A. R. Hutson and D. White, *J. Appl. Phys.* **33**, 40 (1962).
- ³²N. W. Emanetoglu, J. Zhu, Y. Chen, J. Zhong, Y. Chen, and Y. Lua, *Appl. Phys. Lett.* **85**, 3702 (2004).
- ³³V. Chivukula, D. Ciplys, M. Shur, and P. Dutta, *Appl. Phys. Lett.* **96**, 233512 (2010).
- ³⁴Y. J. Guo, C. Zhao, X. S. Zhou, Y. Li, X. T. Zu, D. Gibson, and Y. Q. Fu, *Smart Mater. Struct.* **24**, 125015 (2015).
- ³⁵F. Taleb and S. Darbari, *Phys. Rev. Appl.* **11**, 024030 (2019).
- ³⁶M. Farhat, S. Enoch, S. Guenneau, and A. B. Movchan, *Phys. Rev. Lett.* **101**, 134501 (2018).
- ³⁷A. Sukhovich, B. Merheb, K. Muralidharan, J. O. Vasseur, Y. Pennec, P. A. Deymier, and J. H. Page, *Phys. Rev. Lett.* **102**, 154301 (2009).
- ³⁸D. J. Winarski, E. Kreit, E. M. Heckman, E. Flesburg, M. Haseman, R. S. Aga, and F. A. Selim, *J. Electron. Mater.* **47**, 949–954 (2017).
- ³⁹Y. Takahashi, M. Kanamori, A. Kondoh, H. Minoura, and Y. Ohya, *Jpn. J. Appl. Phys.* **33**, 6611–6615 (1994).
- ⁴⁰J. Bao, I. Shalish, Z. Su, R. Gurwitz, F. Capasso, X. Wang, and Z. Ren, *Nanoscale Res. Lett.* **6**, 404 (2011).
- ⁴¹B. H. Fisher and D. C. Malocha, *IEEE Trans. Ultrason. Ferroelectr. Freq. Control* **57**, 698–706 (2010).
- ⁴²C. Fu, K. J. Lee, K. Lee, and S. S. Yang, *Smart Mater. Struct.* **24**, 015010 (2015).
- ⁴³K. K. Lee, Y. Luo, X. Lu, P. Bao, and A. M. Song, *IEEE Trans. Nanotechnol.* **10**, 839–843 (2011).
- ⁴⁴G. K. Lee, J. H. Moon, and B. T. Lee, *Semicond. Sci. Technol.* **21**, 971–974 (2006).